Journal of Materials Chemistry A

ROYAL SOCIETY OF CHEMISTRY

PAPER

View Article Online
View Journal

Cite this: DOI: 10.1039/d5ta10109c

Pitfalls in parameters: practical process development in chemical vapor processing of SiC†

Benjamin W. Lamm, *[a] Valencia Ramirez, ‡[a] Alex Rogers [b] and Takaaki Koyanagi [a]

Vapor processing of high-value materials, such as silicon carbide (SiC), is of interest for many industries, including aerospace and energy production. Chemical vapor infiltration (CVI) of additively manufactured components is an especially attractive manufacturing process currently in development. Here, a novel development workflow is demonstrated with the H_2–CH_3SiCl_3 gas system for SiC to accelerate the process optimization of CVI SiC. A combination of calculated thermodynamics and high-throughput experimental chemical vapor deposition (CVD) coatings substantially reduced the experiments required with slow CVI processes. The computational results accurately predicted changes in the thermodynamic conditions tested, while CVD coatings – characterized by Raman spectroscopy – addressed changes in kinetic parameters. This workflow is also applicable to other vapor-processing systems, such as pyrolytic carbon, ZrC, or Si_3N_4.

Received 10th December 2025
Accepted 6th March 2026

DOI: 10.1039/d5ta10109c

rsc.li/materials-a

1 Introduction

High-purity SiC produced by vapor-processing methods is of interest for extreme environment applications in nuclear and aerospace industries,[1,2] including the densification of additively manufactured ceramics.[3] Vapor processing, either as coatings by chemical vapor deposition (CVD) or densification of porous materials by chemical vapor infiltration (CVI), is sensitive to processing conditions. Knowledge of the gas-phase and surface chemical reactions occurring in a process is instrumental in understanding the relationship between changes in process variables and changes in the microstructure or composition of the final component. Without such an understanding, operators working in non-optimal parameter space can only guess at the correct changes to make to improve the quality of products – trapped by pitfalls in parameters.

Here, chemical kinetics and thermodynamics will be used to improve the quality of SiC coatings and components formed by vapor processing under two distinct growth regimes. Importantly, developments under "CVD" conditions – typically higher growth temperatures and short run times (hours)-will be used to predict trends under "CVI" conditions – at relatively low temperatures and long run times (days). The proposed development workflow is divided into three parts: (I) thermodynamic system evaluation, (II) experimental evaluation of kinetics by CVD, and (III) experimental CVI validation. Commercial thermodynamics software using standardized databases enables the rapid evaluation of millions of process condition combinations, which can be analyzed to define initial regions of interest. Experimental investigations are necessary to confirm the observed thermodynamic trends identified in Step (I) and to identify any kinetic products or contributions to the reaction mechanism. Critically, by using CVD coatings in Step (II) instead of CVI, the experimental time and consumption of reactants can be reduced by orders of magnitude compared to running the same series of experiments directly in CVI. Finally, the observed trends in kinetics and thermodynamics identified in Steps (I) and (II) can be used to make educated adjustments to the target CVI reactor to attain the desired material composition. This workflow will be demonstrated for the development of CVI SiC.

The most common precursor system used for vapor-processed SiC is H_2-MTS (methyltrichlorosilane, CH_3SiCl_3). MTS is a single-source precursor that contains a 1 : 1 ratio of carbon and silicon, is relatively nonhazardous, and is liquid at room temperature, making it easier to handle than other compounds – *e.g.*, silane.[4,5] Perhaps the most complete

[a]*Materials Science and Technology Division, Oak Ridge National Laboratory, Oak Ridge, TN, USA. E-mail: lammbw@ornl.gov*

[b]*Nuclear Energy and Fuel Cycle Division, Oak Ridge National Laboratory, Oak Ridge, TN, USA*

‡ Present address at School of Chemical and Biomolecular Engineering, Georgia Institute of Technology, Atlanta, GA, USA.

mechanism for H_2-MTS CVD SiC has been developed by the Langlais group.[6–8] Langlais and coworkers present a Langmuir–Hinshelwood surface reaction mechanism for the formation of SiC,[7] summarized in Scheme 1. MTS decomposes to trichlorosilane-radical and methyl-radical species (notated as $^{\bullet}SiCl_3$ and $^{\bullet}CH_3$), which preferentially bind to carbon and silicon surface sites, respectively,[9] reversibly forming single-site $-SiCl_3$ and $-CH_3$ surface species. Neighboring $-SiCl_3$ and $-CH_3$ species can react stepwise to release HCl and form solid Si and C, regenerating silicon and carbon surface sites ($*_{(Si)}$ and $*_{(C)}$). Notably, H_2 is not involved in this reaction mechanism. In the absence of hydrogen (*i.e.*, MTS alone or MTS + inert gas), gas-phase reactions between carbon species form a series of reactive hydrocarbons that can bind to the surface and decompose to free carbon – ultimately forming carbon or C + SiC.[10–12] This reaction path is indicated in Scheme 1 by red arrows; hydrocarbons up to C_2H_x are shown, although species as heavy as benzene (C_6H_6) or larger hydrocarbons can also form from methane.[13,14] However, excess H_2 is also detrimental to the formation of SiC, as indicated by the blue arrows in Scheme 1. Hydrogen can react with $^{\bullet}CH_3$ to form less-reactive CH_4, although methane has been indicated as a direct reactant in the formation of pyrolytic carbon.[13,14] Concurrent with the suppression of carbon deposition, H_2 can react with $^{\bullet}SiCl_3$ to form $SiCl_2$. Dichlorosilane binds to two surface sites as a bridging species and reacts with gaseous hydrogen *via* Eley–Rideal kinetics to form free Si.[7,15,16]

Notably, the $SiCl_2$-formation reaction is slower than the radical reactions; therefore, the $SiCl_2$-formation pathway becomes more significant at longer residence times.[7] The residence time, τ_{res}, at a given position along a cylindrical reactor tube can be determined by (eqn (1)):[17]

$$\tau_{res}(\text{ms}) = \frac{\text{reactor volume}}{\text{volumetric flow}} = 60\,000\frac{\text{ms}}{\text{min}} \times \frac{\pi r^2 \cdot d}{\text{total mass flow}} \times \frac{273\ \text{K}}{T_{dep}} \times \frac{P_{dep}}{760\ \text{torr}} \quad (1)$$

where the tube cross-sectional radius, r, and distance within the hot zone, d, are in cm, the total mass flow is in standard cubic centimeters (sccm), and the deposition temperature (T_{dep}) and pressure (P_{dep}) are in Kelvin and torr, respectively. For a given position in a fixed reactor geometry, τ_{res} can be adjusted proportionally to P_{dep} or inversely to T_{dep} and the total mass flow rate of gases.

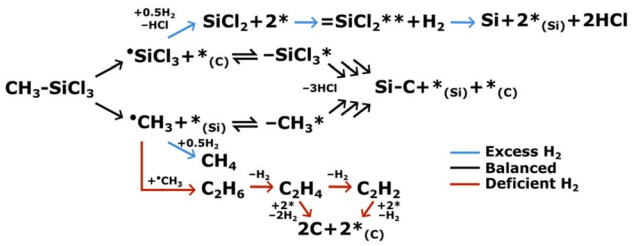

Scheme 1 Decomposition and surface reaction of MTS to SiC. The impact of increased (decreased) P_{H_2} is shown by the blue (red) reaction arrows. Surface sites available for adsorption of gas species are indicated by (*).

While the H_2-MTS system for SiC growth is one of the best understood vapor-processing systems,[18] utilizing that information in process development remains challenging in the face of the wide variety of reactor designs and possible processing conditions. The following sections will (i) use calculated thermodynamic equilibrium to predict changes over a wide variety of reaction temperatures, pressures, and gas ratios and (ii) examine the use of the baseline reaction mechanisms presented in this introduction and varied experimental deposition parameters to alter the composition of the condensed phase formed by vapor processing H_2-MTS at reduced pressure and either 1000 °C (CVI) or 1200 °C (CVD), ultimately targeting the growth of high-purity and crystalline SiC. This study will additionally demonstrate how relatively rapid CVD processes can be used to develop CVI processes, substantially reducing the time required to experimentally determine processing conditions. While this work focuses on the H_2-MTS system for SiC growth, the approach presented here can be extended to other vapor-processing systems.

2 Experimental and computational methods

2.1 Calculation of phase diagrams

CALculation of PHAse Diagrams (CALPHAD) was used to produce equilibrium phase diagrams of the MTS/H_2 system. These were calculated in FactSage 8.2 using a combination of the FactPS and SGTE Solutions 2022 databases. Equilibrium was calculated for 185 gas species, 36 pure liquids, 8 pure solids, 1 liquid solution, and 22 solid solutions. Phase diagrams were calculated with 25 °C steps in temperature from 700 to 1325 °C and 10 torr steps in pressure from 20 to 760 torr.

2.2 Chemical vapor processing

Chemical vapor processing is defined here as synthetic processes using gaseous or vaporized reactants to form solid products, typically on or within a heated substrate. This can be subdivided into coating processes, such as CVD, and densification processes, such as CVI. The CVD and CVI processes used in this study are schematically compared in Fig. 1.

In Fig. 1, CVD coating is shown on a dense substrate (such as a graphite disk, shown in black) in a "cold-wall" reactor. In this scenario, the substrate is inductively heated by an external RF field, radiatively heating the gas stream, as indicated by the yellow area around the black substrate. Reactant gases impinge on the substrate and flow past, primarily coating the front and sides – generally, the back face can become coated as well, although in a thinner coating. In comparison, CVI densification is schematically shown in a "hot-wall" reactor. In this scenario, a conventional tube furnace radiatively heats the reactor tube along an extended area containing the substrates, shown by the yellow area in Fig. 1. The substrates in this case are porous bodies, such as binder-jet-printed SiC pyramids or cones. Reactant gases flow into the hot zone and impinge on the

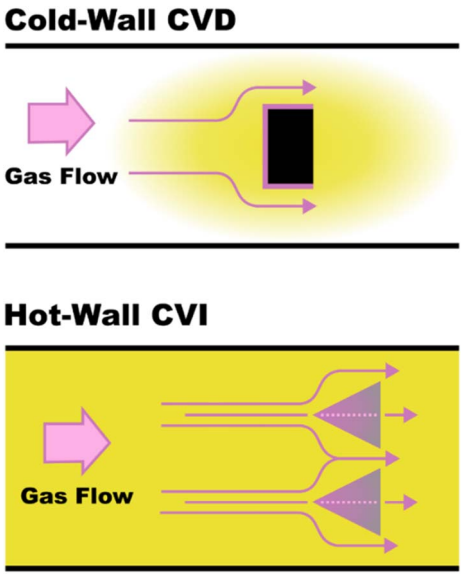

Fig. 1 Schematic comparison of CVD and CVI processes used in this study.

substrates – while a large portion of the gas flows past the substrates, some of the gas diffuses into the substrate, where it deposits and densifies the material.

Importantly, these schemas do not completely represent CVD and CVI processes. CVD often occurs within hot-wall reactor designs and can occur on porous substrates – for example, when seal-coating composite tubes.[19] Likewise, CVI can utilize cold-wall reactors but is limited to porous bodies as substrates. Critically, the largest differences between CVD and CVI for a given gas system are the specific reaction parameters selected. Typically, CVI occurs at temperatures lower than those for CVD to reduce the rates of reaction for both homogeneous gas-phase reactions and heterogeneous surface reactions. Lower temperatures enable the reactant gases to diffuse into porous CVI substrates before reacting on their internal surfaces. Additionally, coating processes grow comparatively much less material than a diffusion-based densification process and thus require much less time (assisted by higher temperatures producing higher growth rates). CVD coatings can typically be completed within hours, whereas CVI densifications require days to weeks, depending on the initial density of the substrate.

In this work, CVI was conducted in a previously described vertical "hot-wall" isothermal, isobaric reactor.[20] Standard infiltrations for SiC use MTS and H_2 in a 1 : 10 ratio at 1000 °C and 200 torr with a total volumetric flow rate of 275 sccm. MTS was introduced to the reactor *via* a bubbler at room temperature (~20 °C) using hydrogen as carrier gas. Substrates were binder-jet-printed SiC powder square pyramids (25 mm base, 25 mm height), and cones (25 mm base diameter, 30 mm height). Printing was performed on an X25Pro (Desktop Metal, USA) using AquaFuse binder (ExOne – now Desktop Metal, USA) and SiC powder (99% purity, median particle size D_{50} = 30 μm, Panadyne – now Arc Impact Acquisition Corp., USA).

CVD was conducted in a previously described horizontal "cold-wall" isothermal, isobaric reactor.[21] Coatings of SiC were grown from MTS-H_2 at 1200 °C at variable precursor ratios and reactor pressures. MTS was introduced to the reactor *via* a bubbler maintained at 25 °C, typically using hydrogen as a carrier gas. Two samples (50-0.2 and 50-4.4; nomenclature described in Section 3.2) used argon as a carrier gas. Substrates were graphite disks (6 mm thick, 19 mm diameter). Deposition temperatures for the inductively heated substrates were set based on an optical pyrometer aimed at a black body hole drilled into the back surface of the substrates. After establishing the desired temperature under flowing argon, the RF power was fixed and held constant during the coating process. By this method, any deviations in substrate temperature due to the coating process (endo- or exothermic reactions) would be apparent and would be consistent with reaction conditions in hot-wall reactors. No significant deviations (>±10 °C) in substrate temperature were noted in the coatings used in this study.

In both CVD and CVI, ultra-high-purity hydrogen and argon were used as received from AirGas (99.999%, AirGas USA). MTS was used as received (TCI, >98.0%).

2.3 Characterization

Following densification, samples were mounted in epoxy, cross-sectioned, and polished to at least 0.5 μm roughness, using colloidal silica on the final polish. Relative densities of densified cone and pyramid samples were measured by the Archimedes method prior to sectioning.

Coating thicknesses of CVD samples were measured from optical micrographs (VHX-6000 digital microscope; Keyence, USA) of polished cross-sectioned samples using ImageJ 1.54 software. Raman spectroscopy of the samples was performed using a confocal LabRAM HR Evolution Raman spectroscope (Horiba Scientific, Japan). The excitation source was a 532 nm monochromatic laser with a lasing power of 6 mW on a specimen. Using a 100× objective lens, the laser spot size was estimated to be 0.25 μm. Raman maps were generated by moving the stage in 1 μm steps and were processed using the χStain principal component analysis software within LabSpec6 (Horiba Scientific, Japan). The χStain application automatically performs data smoothing, background subtraction, and data normalization, and sorts the spectra from each point in the bap based on principal spectral component analysis.

3 Results

3.1 Calculation of phase diagrams

Equilibrium phase diagrams of the MTS-H_2 gas system were calculated at α = H_2/MTS values of 0.5 to 120, where α is calculated as the ratio of initial molar flow rates. A subset of the phase diagrams is shown in Fig. 2, presenting the equilibrium solid products at α = 0.5, 5, 10, and 20 over a range of temperatures and pressures. At low hydrogen concentrations, the calculated equilibrium solid composition across the entire temperature–pressure range presented is a C–SiC mixture (or

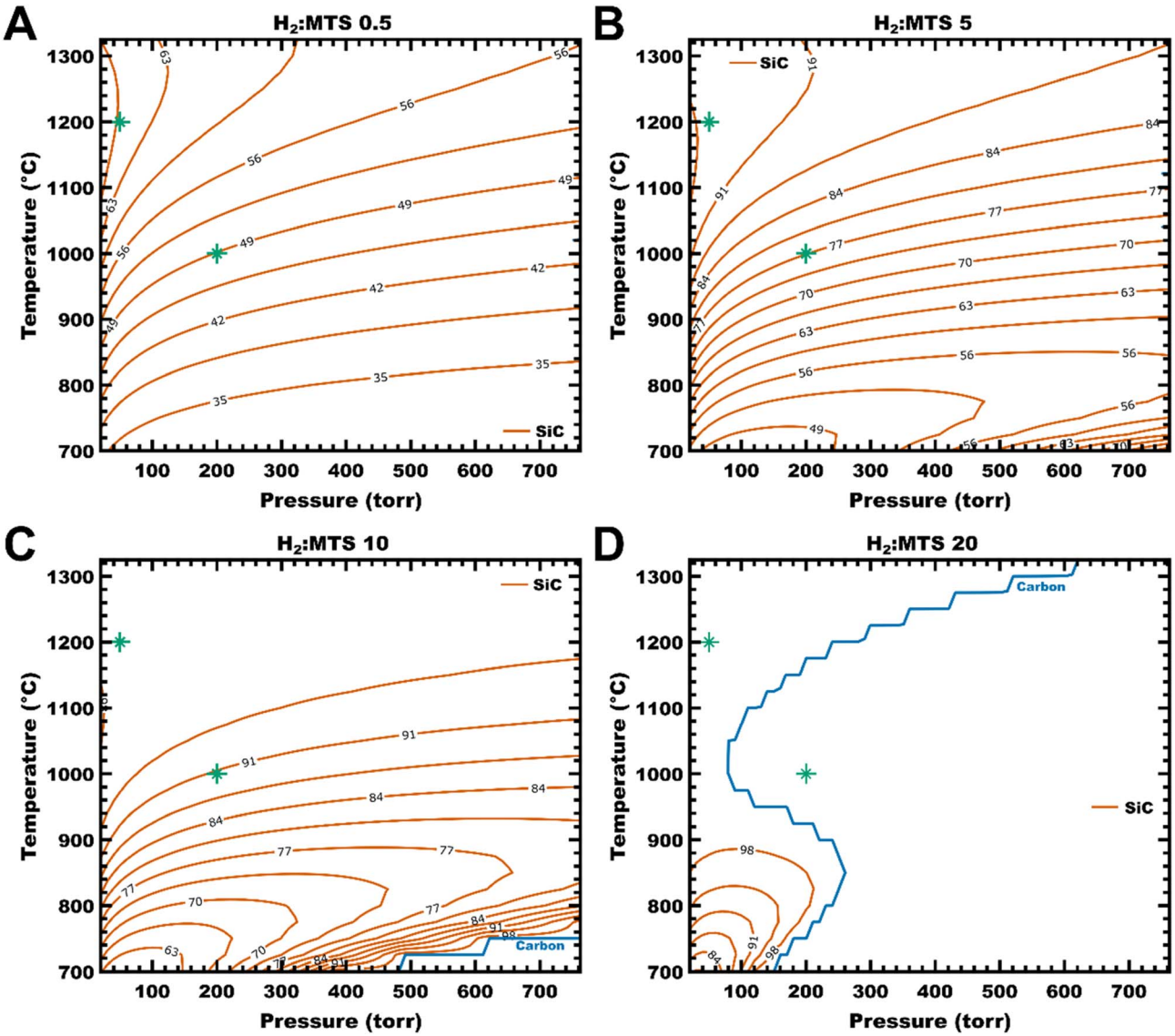

Fig. 2 Calculated phase diagrams of solid products produced from $\alpha = H_2/MTS$ values of (A) 0.5, (B) 5, (C) 10, and (D) 20 over a range of temperatures and pressures. Orange contour lines correspond to amounts of solid products in mole-percent (mol%) of SiC (balance carbon). Blue contour lines indicate the deposition boundary for carbon, *i.e.* the [C/SiC–SiC] (co)deposition transition. Green asterisks (*) mark the experimental conditions used for CVD and CVI SiC.

codeposition), as shown in Fig. 2A and B ($\alpha = 0.5$ and 5, respectively). At $\alpha = 8$, SiC is deposited as a pure product at select temperatures and pressures (initially, low temperatures and high pressures). At $\alpha = 10$ (Fig. 2C), the carbon phase boundary – indicated by a blue line – is seen running nearly linearly from 700 °C/480 torr to 750 °C/760 torr. At lower temperatures and higher pressures than this phase boundary, the condensed phase is predicted to be pure SiC. By $\alpha = 20$ (Fig. 2D), the single-phase SiC deposition occupies over half of the temperature–pressure window presented; at this point, the typical experimental conditions for CVD (1200 °C, 50 torr) are expected to include ~1 mol% free carbon and the conditions for CVI (1000 °C, 200 torr) are expected to produce SiC alone. Experimental CVD and CVI temperature/pressure conditions are indicated in Fig. 2 as green asterisks (*) on the diagrams. Pure SiC from CVD is not expected until $\alpha = 36$; additionally, this temperature–pressure window includes some C–SiC codeposition up to $\alpha = 61$. Notably, the deposition of Si is not predicted over the α-value range examined (0.5–120). Phase diagrams for $\alpha = 8$, 36, 61, and 120 can be found in the SI, Fig. S1.

The calculated equilibrium products at $\alpha = 0.5$ are C and SiC, as shown in Fig. 2A. The amount of SiC increases with temperature across the range of pressures examined up to ~1100 °C; at this temperature, the contour lines become more vertical at 20–200 torr, indicating an increasing effect of pressure changes. At very low pressures (<100 torr), the contour lines are essentially vertical, and changes in pressure dominate the control of solid product composition from 1100 to 1325 °C. This corresponds to the experimental conditions used for CVD; the

calculated composition is *ca.* 35/65 mol% C/SiC. Under the conditions used experimentally for CVI, the solid composition is predicted to be 51/49 mol% C/SiC, with composition affected primarily by system temperature.

Increasing the amount of hydrogen in the initial composition to $\alpha = 5$ (Fig. 2B) increases the amount of SiC produced at equilibrium. Under the CVD and CVI experimental conditions, the topography of solid products is similar to the $\alpha = 0.5$ case – that is, pressure-dependent C–SiC codeposition at high temperature and low pressure and mostly temperature-dependent codeposition at intermediate temperatures and pressures. However, the predicted ratio of materials has shifted towards SiC: ~7/93 C/SiC for CVD and ~23/77 C/SiC for CVI. Additionally, at low temperatures, the contour lines can be seen curving around a C maximum of 52.5 mol% at 700 °C and ~100–200 torr, with increasing amounts of SiC expected to form as pressure increases along the same temperature.

This shift continues at $\alpha = 10$ (Fig. 2C), where the deposition boundary for carbon can be seen running from 700 °C/480 torr to 750 °C/760 torr. At intermediate and high temperatures, the solid product topology is similar to the previous examples, except that the ratio of C/SiC has shifted more towards SiC (~9/91 C/SiC for CVI and 3.5/96.5 C/SiC for CVD). This phase diagram corresponds to the α-value used for CVI SiC in this report, although the solid material deposited is expected to be pure SiC – the variance between calculated thermodynamics and experiment will be discussed in the following sections.

In the final temperature–pressure phase diagram presented here, at $\alpha = 20$ (Fig. 2D), the carbon deposition boundary is now present from 700 to 1325 °C. Under these initial conditions, pure SiC deposition is expected for CVI, but CVD is still expected to codeposit ~1/99 C/SiC. As stated at the start of this subsection, pure deposition of SiC for CVD is not predicted to occur until $\alpha = 36$ (Fig. S1B).

The effect of additional hydrogen (*i.e.*, increasing α) on thermodynamic equilibrium is better understood by examining the equilibrium gas composition as a function of α. Fig. 3 presents the calculated equilibrium gases at CVI and CVD experimental conditions. The gases have been separated generally by cation: Si-containing species in Fig. 3A and D, and hydrocarbons (with some additional species) in Fig. 3B and E.

Under the conditions used here for CVI SiC, the equilibrium amounts of many Si-containing species generally decrease, while hydrocarbon species generally remain constant as α increases (Fig. 3A and B, respectively). This behaviour is largely due to the increase in SiC production and the decrease in free carbon as α increases (Fig. 3C). In a closed system, increasing SiC requires a corresponding decrease in gas-phase Si. In Fig. 3A and B, an inflection point is visible in many Si-containing and hydrocarbon species at $\alpha = 18$ – this corresponds to the carbon deposition boundary, where free carbon is predicted to deposit at $\alpha = 18$ but not at 19. Beyond this inflection point, the equilibrium amounts of Si-containing species generally remain constant or increase (*e.g.*, SiH_3Cl and SiH_4) as a consequence of $SiCH_3Cl_3$ (MTS) decreasing logarithmically with increasing α, while the amount of SiC deposited essentially levels off at $\alpha > 18$. Interestingly, the deposition efficiency of the H_2-MTS system is 99.8% at $\alpha = 0.5$ when considering both carbon and SiC deposition, and decreases to 96.1% at $\alpha = 18$. Above this value, the deposition efficiency increases to 97.0% with increasing α. Increasing the initial amount of H_2 in the system has the general effect of increasing the degree of hydrogenation of Si-bearing species and hydrocarbons – *e.g.*, the equilibrium amounts of CH_4 and C_2H_6 increase up to $\alpha = 18$ and the amounts of SiH_4 and SiH_3Cl increase significantly at $\alpha > 18$. The anticipated impact of increasing the amount of both highly reactive Si-bearing species and stable hydrocarbons will be discussed in the following section.

The evolution of the gas phase with α at the conditions used for CVD reflects the strong shifts in the ratio of products described in Fig. 2. In Fig. 3D, the amounts of most Si-bearing species decrease, with the exception of SiH_2Cl_2, SiH_3Cl, SiH_4, and SiH, which are all reactive species associated with Si deposition.[22–25] The most abundant Si species changes from $SiCl_4$ – a fully-saturated species – to $SiCl_2$ at $\alpha = 2$. Notably, the amount of $SiCH_3Cl_3$ (MTS) at equilibrium has decreased to below 10^{-10} mol at all α-values, and thus is not shown in Fig. 3D, suggesting a much higher reactivity under the CVD conditions compared to the CVI conditions examined here. The composition of hydrocarbons at equilibrium for CVD, shown in Fig. 3E, are largely the same as those for CVI, although the amounts of unsaturated, reactive species (*e.g.*, C_2H_2) are higher, while the amounts of saturated species are much lower (*e.g.*, $CH_4 < 10^{-1}$ mol *vs.* ~0.5 mol or $C_2H_6 < 10^{-10}$ mol *vs.* ~10^{-6} mol at $\alpha = 30$, comparing CVD to CVI), also suggesting higher reactivity for carbon under these conditions. The combination of high reactivities for both Si and C implies a high deposition efficiency, which is supported by the amounts of solids formed, as shown in Fig. 3F. The amount of free carbon decreases significantly by $\alpha = 10$, and the deposition efficiency for total solids (C + SiC) ranges from 99.99% to 99.4% from $\alpha = 0.5$ to 30.

3.2 Experimental results: CVD coatings

The impact of two thermodynamic parameters (α and total pressure) and one kinetic parameter (residence time) on "high"-temperature SiC vapor processing was investigated by varying these parameters for coating a dense graphite substrate. The impact of temperature on the H_2/MTS system for CVD SiC has previously been investigated and was found to primarily affect the growth rate of the coatings.[26–29] The experimental process conditions are listed in Table 1. All samples were coated at a substrate temperature of 1200 °C. Samples are identified by the reactor pressure and α-value used – *i.e.*, sample 50-0.2 was grown at 50 torr and $\alpha = 0.2$. Coating thicknesses were measured from optical micrographs in cross-section. The coating thicknesses for Samples 50-0.2, -4.4, and -6.8 were not measured; thus, the information cannot be included in Table 1. However, the gravimetric growth rates are included for comparison to other samples. Neither coating thickness nor growth rates were included in the present processing analysis, and the omission of these data points was not deemed detrimental to the study.

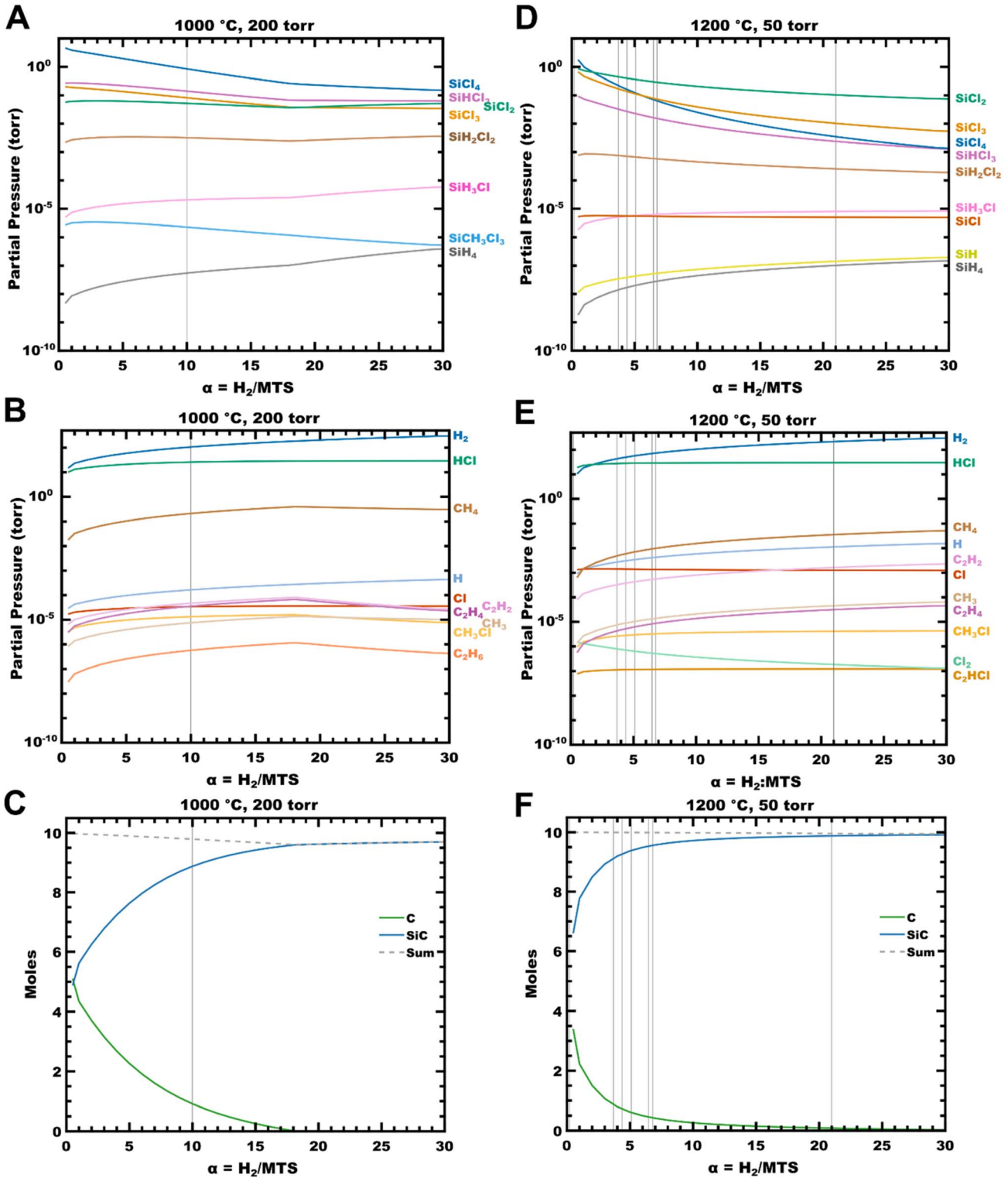

Fig. 3 Gas composition at equilibrium for $\alpha = 0.5–30$ for CVI (A and B) and CVD (D and E) conditions. Moles of solids for CVI (C) and CVD (F) are also presented. Vertical grey lines indicate the experimental α-value(s) used for CVI and CVD (at 50 torr)

Coatings were generally nodular at the surface, while dense and isotropic in cross-section. Coating composition and crystallinity were determined by Raman microscopy; representative spectra are shown in Fig. 4, and reference Raman spectra for single-crystal silicon and commercial CVD 3C–SiC are given in Fig. S2. Coatings predominantly composed of crystalline silicon, such as 700-50 in blue, were easily identified by a single sharp peak at 520 cm^{-1}. In the reference spectrum from sample

Table 1 Process conditions and coating thickness of CVD at 1200 °C. Sample names are defined by the reactor pressure and α-value – *e.g.*, 50-0.2 was run at 50 torr, $\alpha = 0.2$. Effective pressures are shown in parentheses for experiments using Ar in addition to H_2 and MTS

Sample	Total (effective) pressure (torr)[a]	$\alpha = H_2$/MTS	Residence time (ms)	Coating time (min)	Thickness (μm)[b]	Growth rate (mg min^{-1})
50-0.2	50 (3.4)	0.2	287	30	n/m	2.51 ± 0.02
50-3.7	50	3.7	1522	30	40 ± 3	4.52 ± 0.02
50-4.4	50 (15.8)	4.4	1578	30	n/m	5.43 ± 0.02
50-5.1	50	5.1	2453	45	50 ± 6	3.09 ± 0.02
50-6.5	50	6.5	42	15	60 ± 2	14.47 ± 0.05
50-6.8	50	6.8	291	30	n/m	8.17 ± 0.02
50-21	50	21	760	45	31 ± 10	3.66 ± 0.02
50-30	50	30	754	60	33 ± 2	2.02 ± 0.01
375-7.0	375	7.0	706	15	104 ± 4	25.77 ± 0.05
375-25	375	25	1530	30	117 ± 9	11.59 ± 0.02
375-44	375	44	2284	30	55 ± 7	5.98 ± 0.02
700-6.8	700	6.8	1978	15	91 ± 9	23.89 ± 0.05
700-29	700	29	2307	30	132 ± 8	14.06 ± 0.02
700-50	700	50	1527	30	117 ± 4	12.34 ± 0.02
700-53	700	53	765	30	181 ± 47	14.42 ± 0.02

[a] Samples with (effective) pressure indicate samples diluted with argon. Effective pressure calculated from amount of dilution. [b] n/m = value not measured.

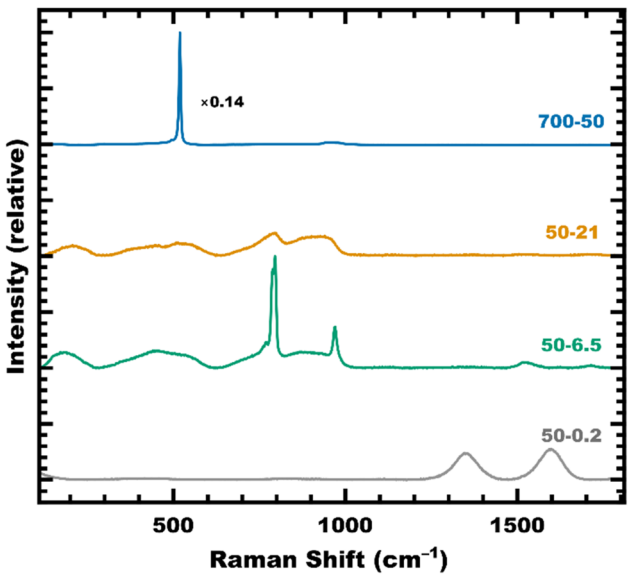

Fig. 4 Representative Raman spectra of CVD coatings. The sample IDs can be found in Table 1.

700-50, the broad low-intensity band at ~960 cm^{-1} is consistent with the 2TO phonon of Si.[30,31] Crystalline SiC coatings, such as 50-6.5 in green, include sharp peaks at ~795 and ~970 cm^{-1}, which correspond to the transverse optical (TO) and longitudinal optical (LO) stretches, respectively, of 3C–SiC.[32] The shoulder at lower wavenumbers on the TO-SiC stretch indicates stacking faults within the crystals.[33] Broad stretches centered at ~180 and ~430 cm^{-1} are consistent with Si–Si stretching caused by crystalline disorder.[34,35] At higher wavenumbers, low-intensity bands at ~1520 and ~1710 cm^{-1} are consistent with two-phonon stretches (2TO and TO + LO, respectively) and are distinctive from the bands observed in graphite (~1330 and 1580 cm^{-1}) or diamond (1332 cm^{-1}).[36,37] Several coatings consisted of disordered SiC (d-SiC), of which 50-21 in orange is one. These d-SiC coatings included broad bands ~200 and 520 cm^{-1} and sometimes at ~1420 cm^{-1}, which are characteristic of Si–Si and C–C homonuclear bonds, respectively.[35] Notably, the TO and LO SiC bands are much broader than for SiC samples (*e.g.*, 50-6.5) and have much lower relative intensity, indicative of a highly disrupted structure.[35] The Raman spectrum from one sample, 50-0.2, showed only broad bands at ~1350 and 1600 cm^{-1}, which correspond to the D and G bands, respectively, of graphite.[36]

The compositions of CVD coatings are presented in Fig. 5, represented as functions of process variables (α, pressure, and residence time). Composition assignments were selected based on the Raman spectra, similar to the data presented in Fig. 4. Where multiple phases or materials are present, the assignment indicates this by multicolored dots – for example, sample 50-5.1 was a mix of crystalline and disordered SiC (d-SiC/SiC) and is represented by a half-orange (d-SiC) and half-green (SiC) circle. Similarly, sample 375-7.0 was a Si/d-SiC/SiC mixture and is represented by a tricolored blue–orange–green circle. Generally, coatings grown at high pressure (375 or 700 torr), moderate to high residence time (>700 ms), and high α (≥25) are crystalline Si. Conversely, crystalline SiC coatings were grown only at relatively low pressures (50 torr), moderate α (6.5–30), and low residence times (<300 ms). The single graphite coating was grown at very low α (0.2), low pressure (50 torr), and low residence time (287 ms). This sample, 50-0.2, was also diluted 93% with ultra-high-purity argon to maintain a low residence time at very low α. Dilution also affects gas chemistry by increasing the mean free pathlength between collisions of C- and Si-bearing species – effectively, decreasing the pressure of the reaction. An effective pressure, P_{eff}, can be calculated from the partial

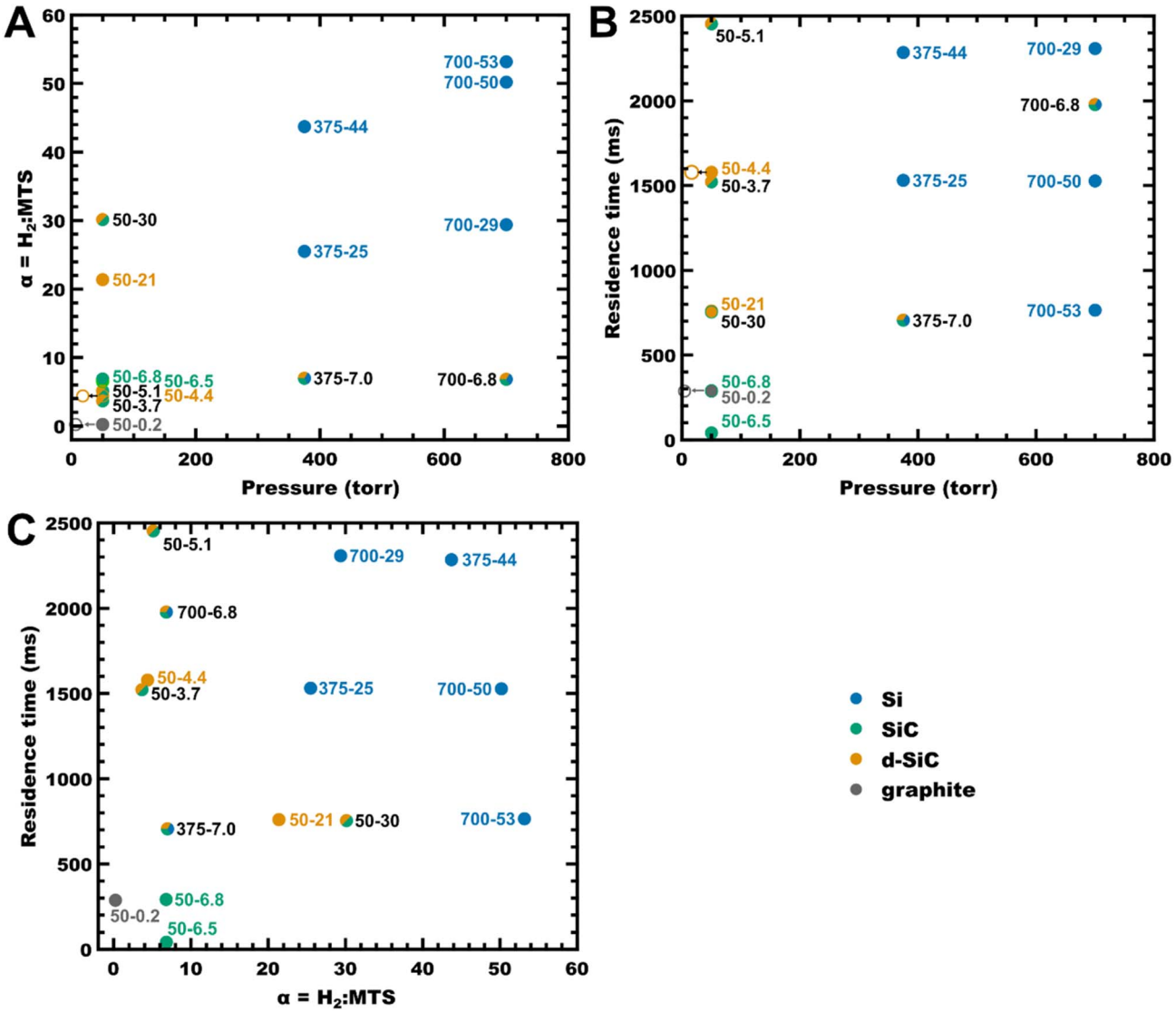

Fig. 5 Composition of CVD coatings as a function of total pressure, $\alpha = H_2/MTS$, and residence time. Graphs are shown for (A) α *vs.* pressure, (B) residence time *vs.* pressure, and (C) residence time *vs.* α. The composition of coatings is indicated by the color of each point; mixed composition samples are shown by multi-color points (*e.g.*, a half-orange, half-green point corresponds to a d-SiC/SiC mixture). The sample IDs can be found in Table 1.

pressures of hydrogen and MTS to estimate the effect of dilution (eqn (2)):

$$P_{\text{eff}} = P_{\text{H2}} + P_{\text{MTS}} = P_{\text{total}} - P_{\text{Ar}} \quad (2)$$

The effective pressures of samples 50-0.2 and 50-4.4 are provided in Table 1 and shown in Fig. 5 as open circles. Several samples were not purely Si, SiC, or d-SiC, but instead showed a mixture of two of these materials (*i.e.*, d-SiC/Si or d-SiC/SiC). Some explanations of these compositions and why similar samples produced different compositions will be discussed further in Section 4.2.

It is worth noting that the use of a cold-wall CVD for this section of the development workflow was particularly useful in accelerating sample turn-over time. Because only the substrate was heated by the RF field, a coating experiment could be started in ~15 min after loading the sample and could be extracted safely ~45 min after ending the experiment. Comparatively, a similar hot-wall reactor design would require ~2 h both before and after the coating process to allow for heating and cooling of the reactor, resulting in a three-hour time saving per coating when using a cold-wall reactor.

3.3 Experimental results: CVI processing

The behavior of the H_2-MTS system was also examined *via* the densification of porous bodies (CVI), by infiltrating two geometries (cones and pyramids). Both shapes were expected to show the effect of infiltration depth and gas flow direction on the densification of porous components. The details of these substrates are described in Section 2.2 and in previous work.[3,20]

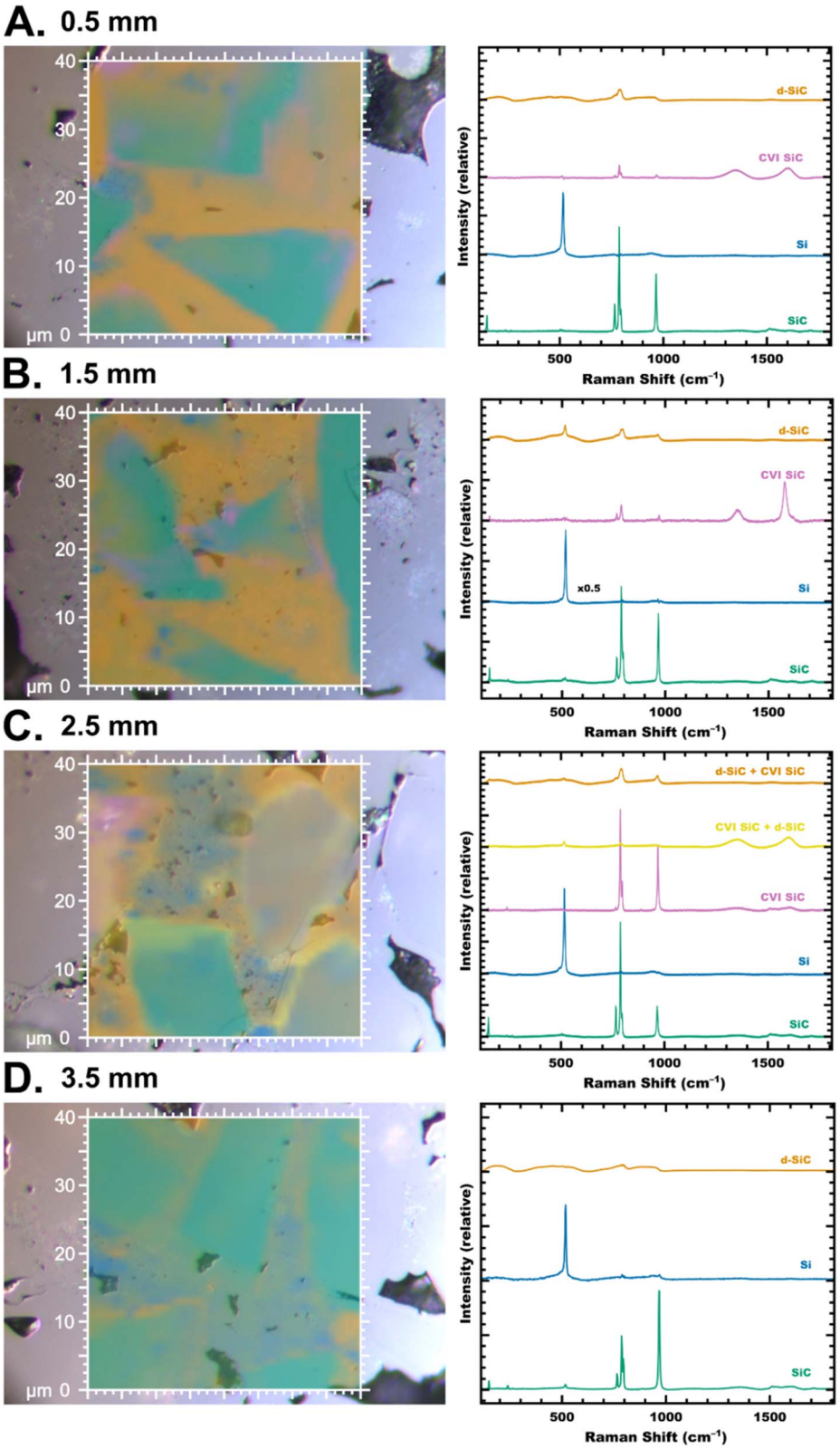

Fig. 6 Raman maps and spectra for printed pyramid infiltrated by standard CVI conditions. Maps are positioned (A) 0.5, (B) 1.5, (C) 2.5, and (D) 3.5 mm from the surface of the infiltrated part. The optical micrographs are the same scale as the Raman maps. The borders of the Raman maps include a scale bar in both *x*- and *y*-axes.

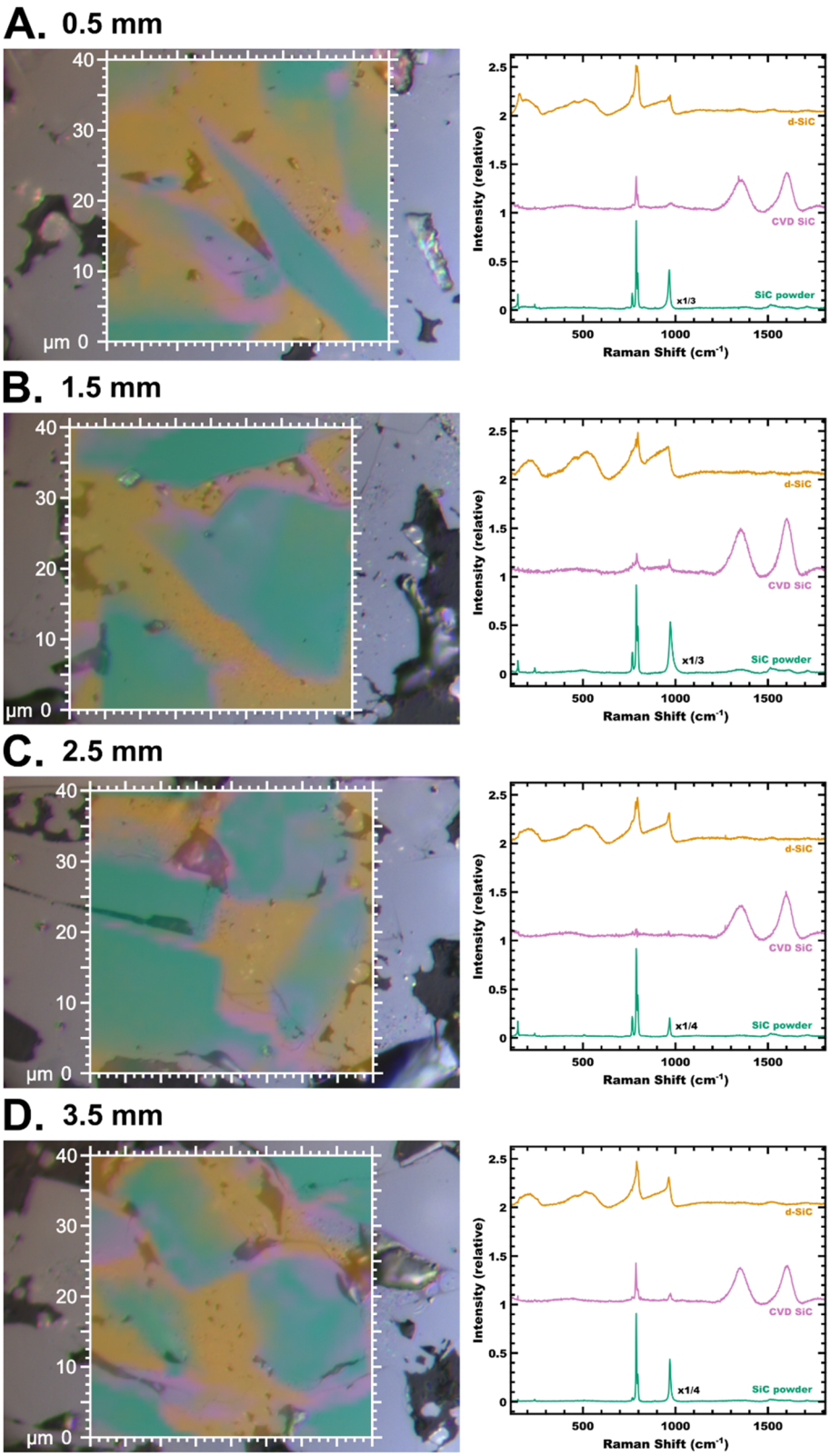

Fig. 7 Raman maps and spectra for printed pyramid infiltrated at shorter residence time CVI conditions. Maps are positioned (A) 0.5, (B) 1.5, (C) 2.5, and (D) 3.5 mm from the surface of the infiltrated part. The optical micrographs are the same scale as the Raman maps. The borders of the Raman maps include a scale bar in both *x*- and *y*-axes.

The binder-jet-printed green bodies had an average geometric density of 38.5 ± 0.6%. Following infiltration, the geometric density increased to 82.1 ± 1.8%, in good agreement with the Archimedes density of 82.4 ± 0.3%. Note that the Archimedes density of as-printed components could not be measured, as the binder used is soluble in both water and ethanol.

To determine the structure of the vapor-grown matrix, the samples were cross-sectioned and polished. The orientation of the samples within the reactor gas flow was visually apparent – the sample bases were less dense than the top and sides. The microstructures and compositions for both samples were very similar, and the results from the pyramid sample are shown in Fig. 6. From optical microscopy, the microstructure was generally consistent and composed of three features: dense polygonal SiC grains (used in the print), dense vapor-grown matrix, and speckled vapor-grown matrix. The SiC grains and dense vapor-grown matrix were visually similar, distinguishable only by the interface between the materials. The "speckled" matrix regions were a lighter shade than the dense matrix. Optical micrographs from different depths within the pyramid sample are shown in Fig. 6; all three microstructures were present at all depths examined, and an example of the speckled matrix structure is especially visible in the upper-right corner of the micrograph at 1.5 mm in Fig. 6B. The composition of the vapor-grown matrix was determined by Raman microspectroscopy; representative spectra for the different phases identified and maps of the phases are shown in Fig. 6.

Throughout the sample, several phases are consistently present. Shown in green, the SiC powder used in the print is identified as 6H–SiC; stretches at 965 cm^{-1} are consistent with the LO mode, at 786 and 764 cm^{-1} with the TO mode, and at 148 cm^{-1} with the transverse acoustic (TA) mode.[32] Crystalline silicon, shown in blue, is distinguishable by the strong stretch at 520 cm^{-1}, as discussed for the CVD coatings section. The "speckled matrix" microstructure is associated with silicon, although silicon was also identified within some "dense matrix" areas. The majority of the dense matrix was identified as d-SiC, shown in orange. Spectra for d-SiC regions contained broad Si–Si stretches at ~200 and ~500 cm^{-1} and broad Si–C stretches at ~900 cm^{-1}, as well as a low-intensity TO-SiC peak at ~800 cm^{-1} – the d-SiC spectrum in Fig. 6A is a good representation.[35]

Some crystalline vapor-grown SiC was identified, as shown in pink. Spectra for these regions generally contain LO and TO stretches of SiC, as well as the D and G peaks of graphite at 1350 and 1600 cm^{-1}. Crystalline vapor-grown SiC was primarily identified at the surface of SiC print particles, suggesting that the particles acted as crystallization sites for the growing material. The polytype grown is indeterminate, but likely contains many stacking faults based on the positions of the LO and TO peaks – for example, in Fig. 6C, the CVI SiC peaks are at 968 cm^{-1} and 786 cm^{-1} with a shoulder at 795 cm^{-1}.[38] The TA stretch of 6H–SiC at 148 cm^{-1} is absent, suggesting this phase is distinct from the SiC print particles. Defect-rich 3C–SiC grown by vapor processing has been reported previously,[33,39] and the type and concentration of defects in the current samples could be further characterized by STEM, SAED, or EBSD techniques.

Some regions were composed of mixtures of phases, such as in the d-SiC region of Fig. 6B (containing some Si in addition to d-SiC) or in Fig. 6C ("d-SiC" contains low-intensity LO and TO

Table 2 Process conditions of standard and adjusted CVI at 1000 °C and 200 torr

CVI	Infiltration time (h)	H_2 flow (sccm)	MTS flow (sccm)	$\alpha = H_2$/MTS	Residence time (s)
Standard	93	250	23.8	10.5	11.46
Adjusted	67	350	30.0	11.7	8.26

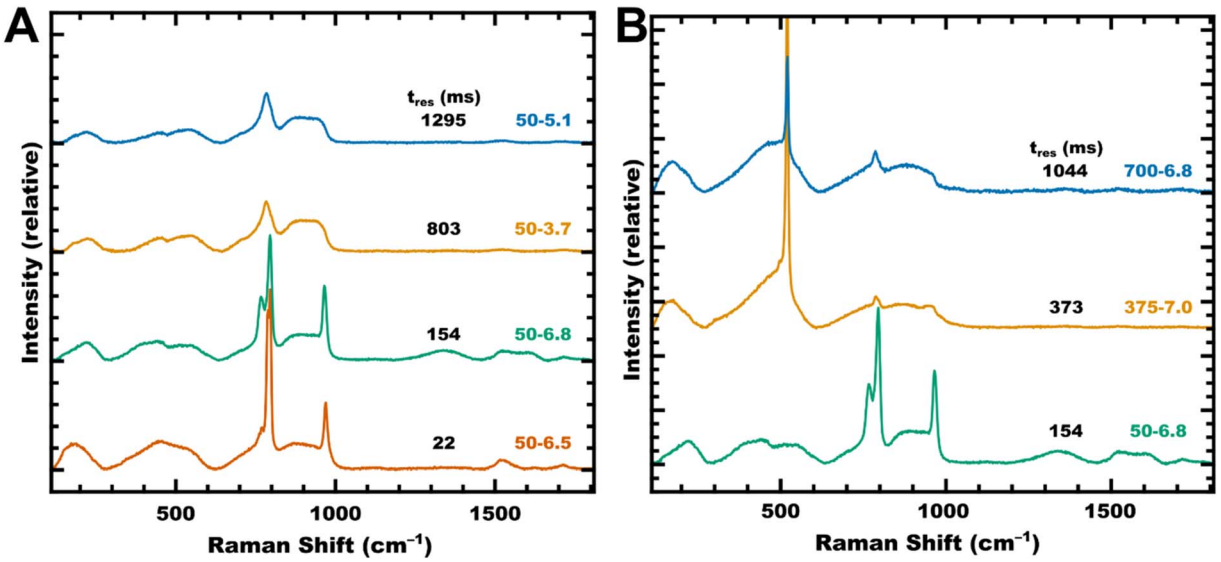

Fig. 8 Raman spectra of mixed-composition and comparable samples for (A) d-SiC/SiC and (B) Si/d-SiC/SiC coatings. The sample IDs can be found in Table 1.

stretches; "d-SiC + CVI SiC" in yellow contains the stretches for Si, LO- and TO-SiC, and D and G of graphite).

Notably, the crystalline silicon was identified at all depths investigated, suggesting that the active species present during vapor processing promote Si deposition. Accordingly, it was recommended that the process conditions be altered to decrease residence time by (i) lowering pressure, (ii) increasing temperature, or (iii) increasing total mass flow. The infiltration pressure is currently a fixed parameter in the reactor design. The infiltration temperature has previously been optimized to minimize growth rate while maintaining a crystalline deposit. Therefore, the experiment was repeated by increasing the total mass flow rate, thereby decreasing the residence time from 11.46 s to 8.26 s.

Raman maps from the samples produced under adjusted CVI conditions are presented in Fig. 7. The specific parameters used in the CVI samples are listed in Table 2. Under the adjusted conditions, Raman maps indicate a similar mixture of SiC powder with a d-SiC and crystalline SiC matrix. At positions measured, the matrix consists primarily of d-SiC; however, crystalline Si is notably absent. Changes in d-SiC are also apparent. The d-SiC phase present under standard CVI conditions (Fig. 6) is generally low in intensity with peaks only at $\sim$780 cm^{-1}, consistent with the TO mode of SiC. The d-SiC spectrum at 1.5 mm (Fig. 6B) additionally includes a peak at 520 cm^{-1}, indicative of Si crystallinity. In comparison, the d-SiC spectrum for adjusted CVI has a higher relative intensity than the "standard CVI" spectrum. The adjusted CVI d-SiC spectrum includes peaks at $\sim$780 and $\sim$970 cm^{-1}, corresponding to and LO modes in SiC. Overall, this suggests increased Si–C bonding using adjusted CVI parameters compared to the standard CVI conditions.

To further increase the amount of crystalline SiC grown, the residence time should be reduced further – either by increasing the total flow rate more or by adjusting the equipment to permit lower operating pressures. Alternatively, the total system pressure could be maintained by diluting the H_2/MTS flow with argon; however, this would also require equipment alterations and is beyond the scope of the present study.

4 Discussion

The following discussion will present the analysis and conclusions of the results presented in Section 3. The results of the calculated phase diagrams will be contextualized based on the limitations of using thermodynamic equilibrium to predict the results of dynamic systems, including how the calculated results hint at the formation of kinetic products (*i.e.*, free silicon) despite not predicting free Si growth, and how these phase diagrams can be utilized to adjust the composition of experimental products. The results of CVD coatings will also be discussed, focusing primarily on mixed compositions and trends observed when deposition variables are altered. A final note on the optimal conditions for SiC growth in the experimental reactor used here is also included. Finally, the infiltration and densification of porous bodies are discussed, focusing on the importance of relative gas volume and surface area. Notably, the volume-to-surface area ratios between CVD-coated samples and CVI densification are similar in this study, meaning that parametric trends observed in CVD coatings should be consistent with CVI.

The combination of both thermodynamic and kinetic variables – temperature, pressure, and initial gas ratio (α) in the former case, and residence time τ_{res} in the latter – results in a large combination of variables that are critical for the development of high-purity vapor-processed materials, producing a pitfall in parameters. Using a combination of thermodynamic modeling and experimental development in a similar, though rapid, process – such as CVD – can be used to develop CVI processes.

4.1 Validation of calculated thermodynamic equilibrium

As noted in Section 3, there are several cases where the calculated thermodynamic results deviate from experimental results, presented both here and in previous literature. CALPHAD is a method to generate equilibrium phase diagrams of a chemical system based on minimization of Gibbs free energy – in this case, the H–C–Si–Cl system, also referred to here as the H_2-MTS system, based on the initial gas chemistry. Because CALPHAD is a purely thermodynamic approach, some features that are very significant in real-world, experimental systems are missing. For example, CALPHAD systems are essentially static environments – the atom inventory of the system remains constant; in comparison, a dynamic system such as CVD or CVI removes gaseous species. Minimization of Gibbs free energy also does not include any time-dependent terms – indeed, molecular kinetics are not even considered. Consequently, reactions that would normally be so slow as not to occur in a real system are predicted to occur in CALPHAD. Despite these drawbacks, CALPHAD is a useful methodology to predict trends in chemical systems, and has historically been successfully used for this purpose for SiC oxidation and corrosion,[40] CVD codeposition of ZrC–SiC,[21] and thermomechanical property development,[41] to name a few examples. However, the lack of kinetic considerations does require discussion.

In the H_2-MTS system, experimental initial gas ratios of α = 5–10 are often reported as successfully producing pure SiC;[28,33,42] additionally, SiC–Si codepositions – up to nearly-pure Si – have been reported at $\alpha > 10$, typically in combination with higher total pressures.[10,43] In contrast, the equilibrium phase diagrams presented here do not predict the formation of Si at any condition up to the limit of examined gas ratios, $\alpha = 120$, and C–SiC codeposition is predicted up to $\alpha = 18$ for the temperature–pressure combinations examined experimentally for CVI in this study. Because of this disconnect between CALPHAD and experimental results, the determination of the α-value where Si formation begins will depend significantly on the residence time of the reactor used, thus requiring experimental investigation. Importantly, the CALPHAD results showing a decrease in deposited carbon and an increase in SiC suggest that Si-rich phases are promoted at higher pressures and low temperatures, in agreement with previous work.[44–48]

The changes to the equilibrium gas compositions predicted by CALPHAD for CVI and CVD temperatures and pressures are also consistent with experimental results demonstrating deposition of free Si at high α-values. As mentioned in Section 3.1, stable or less-reactive Si-bearing gas species decrease (*e.g.*, $SiCl_4$, MTS), whereas species associated specifically with crystalline Si growth increase (*e.g.*, SiH_4, SiH_2Cl_2, SiH_3Cl, $SiCl_2$).[15] Notably, the equilibrium concentration of $SiCl_3$, which has been associated with crystalline SiC growth,[7] decreases with increasing α at both temperature–pressure conditions investigated here. Additionally, the equilibrium concentration of saturated hydrocarbons increases with α-value, especially at 200 torr and 1000 °C ("CVI" conditions). As shown in Fig. 2B, methane (CH_4) is the dominant hydrocarbon at ~0.5 torr – the next-highest partial pressures are for C_2H_4 and C_2H_2 (reactive species at $\sim10^{-4}$ torr and $\alpha = 18$).[13,49,50] The concentration of ethane (C_2H_6) – another saturated and nonreactive hydrocarbon – is also significant (10^{-7} – 10^{-6} torr). As α increases past the carbon deposition phase boundary of $18 < \alpha < 19$ described in Section 3.1, the partial pressures of all hydrocarbons decrease, except for CH_4, which remains constant. Notably, at 1200 °C and 50 torr ("CVD" conditions), the overall trends of hydrocarbons with α are consistent, but the relative amounts are significantly different compared to CVI conditions. Methane is still the highest-partial-pressure hydrocarbon, but the maximum pressure is < 0.1 torr. The partial pressures of CH_3 and C_2H_2 are ~10–100× higher in CVD than in CVI conditions across α-values, while the partial pressure of C_2H_6 is $< 10^{-10}$ torr under CVD conditions (thus not shown) at all α-values investigated. Overall, as α increases, the growth of (free, crystalline) Si is promoted, while the growth of C (as SiC or graphite) decreases. Additionally, at higher pressures and lower temperatures (CVI conditions *vs.* CVD conditions discussed here), the trend is more significant, suggesting again that free Si growth is most likely to be initiated at higher pressures and lower temperatures for a given α-value condition.

In summary, as pressure and/or α-value increases, the concentration of reactive Si-bearing gas species increases, while the concentration of reactive C-bearing gas species decreases. In a dynamic system (such as CVD or CVI), the growth of Si will dominate at higher pressures and α-values. The real-world equivalent to the CALPHAD model would essentially be a static system (*e.g.*, a closed chamber) held at elevated temperatures for an extended period. In this scenario, silicon would still be expected to form first due to the aforementioned relative gas kinetics between the dominant Si-bearing and C-bearing species. Next, carbon would grow on exposed surfaces as the hydrocarbon species either react directly with the substrate or proceed through gas-phase reactions with hydrogen to form more reactive unsaturated or aromatic hydrocarbons.[14,51] Given enough time for diffusion,[52–55] the equilibrium product of SiC would form from Si and C layers.

4.2 CVD coatings: analysis of mixed compositions

Several coatings had mixed compositions – either d-SiC/SiC (50-3.7, 50-5.1, 50-6.8, 50-6.5) or Si/d-SiC/SiC (375-7.0, 700-6.8); the Raman spectra for these coatings are shown in Fig. 8. The d-SiC/SiC compositions, shown in Fig. 8A, include the TO stretch of SiC at ~800 cm^{-1}, and in the case of 50-6.5 and -6.8, the LO stretch of SiC at ~970 cm^{-1}. The background of these samples is composed of broad bands at ~200 and ~500 cm^{-1} – Si–Si stretching – and a broad band at ~900 cm^{-1} attributed to non-crystalline Si–C stretching.[35]

In terms of total pressure and α-value, samples 50-3.7, -5.1, -6.5, and -6.8 are all very similar, but were found to vary in composition. All four samples include wide bands associated with disordered Si–Si (~200 and ~500 cm^{-1}) and Si–C (~900 cm^{-1}) stretching;[35,56] however, where samples 50-6.5 and -6.8 contained sharp peaks at 795 and 970 or 965 cm^{-1} (respectively), indicative of crystalline SiC, samples 50-3.7 and -5.1 were observed to have only wide peaks at ~783 cm^{-1}, indicative of less-organized Si/C compositions; therefore, 50-3.7 and -5.1 were qualitatively assigned as d-SiC/SiC mixtures. The increase in α likely contributed to the general increase in the crystalline SiC nature of these coatings; however, the differences in residence time were more significant. Both of the SiC samples had residence times <300 ms, compared to τ_{res} for 50-3.7 and -4.4 of ~1550 ms and for 50-5.1 of 2453 ms. These large increases in residence time have been calculated to produce higher concentrations of Si-forming species (*e.g.*, $SiCl_2$) and lower concentrations of SiC-forming carbon species (*e.g.*, CH_3), as discussed both in the present work and in the literature.[57] The crystallinity of SiC also improves as τ_{res} decreases – 50-6.8 has peaks at 965 and 795 cm^{-1}, with a shoulder at 766 cm^{-1}, while 50-6.5 has peaks at 970 and 795 cm^{-1}. In the latter case, the spectrum for 50-6.5 is a good match for 3C–SiC, while the spectrum for 50-6.8 is intermediate between those of 3C- and 6H–SiC.[32] The shift in the SiC LO peak (~965 cm^{-1}) has previously been associated with disordered atomic stacking.[56]

On the other side of the composition transition, Si/d-SiC/SiC mixtures were found for samples 375-7.0 and 700-6.8, as shown in Fig. 8B. In these samples, the strong crystalline Si peak at 519 cm^{-1} is apparent, along with broad Si–Si stretches at 200 and 500 cm^{-1}, Si–C stretches at ~900 cm^{-1}, and short peak(s) for SiC TO and (for 375-7.0) LO modes. In comparison, the spectrum from sample 50-6.8 includes a sharp SiC TO peak at 795 cm^{-1} (with a strong shoulder at 766 cm^{-1}) and a single LO peak at 965 cm^{-1}. The background stretches at ~200 and ~500 cm^{-1} (Si–Si) and those at ~900 cm^{-1} (Si–C) are consistent with d-SiC and have previously been observed in vapor-grown SiC samples.[1,35] For highly crystalline vapor-processed SiC, the background features have also been attributed to the effect of ultra-fine grain size on the Raman spectra.[58,59] All three of these samples – 50-6.8, 375-7.0, and 700-6.8 – have nearly equivalent α, but increase in both pressure (50, 375, and 700 torr, respectively) and residence time (291, 706, and 1976 ms, respectively). Increasing pressure or residence time is expected to increase the rate of gas-phase reactions, increasing the concentration of Si-forming species (*e.g.*, $SiCl_2$).

For the cold-wall CVD reactor used in this study at 1200 °C, there appears to be a parameter window for SiC formation between $\alpha = 4$ and 8, residence time τ_{res} < 300 ms, and total pressure 50 torr. Higher pressures might be accessible at $\alpha < 6.5$

or lower τ_{res} – the minimum residence time tested here at 375 and 700 torr was ~700 ms. Higher total pressures should also be accessible by adding inert gas (*e.g.*, Ar) to dilute the reactants – a strategy that is useful when total flow rates are important (such as in fluidized beds) or when very large reactors are used (such as in industrial environments). Previous studies have also demonstrated that increasing deposition temperature promotes the growth of crystalline SiC,[44–48] with temperatures of 1300–1600 °C being especially productive.

Future work focused on improving the characterization of vapor-processed materials would benefit the workflow of this process. Specifically, methods of quantifying the various crystalline and amorphous phases would improve the refinement of experimental phase diagrams. Quantified composition information can also be used as training material for machine learning algorithms, which could expedite process development.

4.3 Parallels between CVI components and CVD coatings

Vapor coating dense substrates depends primarily on total pressure, temperature, and residence time. When infiltrating porous bodies, the impact of the relative gas volume and surface area (V/S) can also become significant. This concept has been demonstrated experimentally for the growth of pyrolytic carbon (PyC)[60,61] and has been described more conceptually elsewhere.[62] In their experiment comparing volume to surface area,[60] Hüttinger *et al.* compared substrates with a 23-fold change in V/S, which was enough to shift growth kinetics from dominance of gas-phase homogeneous reactions (at high V/S) to dominance by heterogeneous surface reactions (at low V/S). Critically, this "CVD" experiment and subsequent "CVI" experiments by the Hüttinger group used porous substrates that filled the entire cross-section of the reactor tube.[61] This fact is important for two reasons: first, that the calculated V/S ratio considers the volume of the entire heated volume, not just the change in V/S of individual substrates; and second, that, in the Hüttinger group's "CVI" series, reaction gases are largely forced through the porous body instead of flowing past or around it. In the present study, relatively small porous substrates (~5 cm^3) were located in a relatively large volume (~1800 cm^3 heated volume); accordingly, while the available surface area is much higher in the as-printed pyramids and cones compared to dense monoliths of the same external dimensions, the overall change in V/S is relatively small. Additionally, the present experimental setup allows gas to flow past the porous substrates. This particular set-up is favorable for the densification of many small parts, compared to a force-flow CVI producing single dense parts per batch.

The Hüttinger group also investigated the effect of residence time on the densification of porous bodies.[50,61,63,64] Their results, studying CVI PyC from $Ar/H_2/CH_4$, demonstrated interesting trends in densification, where the rate of densification increased from the pore surface inward at low residence times ('backfilling' porosity) and, at high residence times, having an inverse gradient (closing off internal porosity or skinning at the surface). These results are highly specific to the chemistry of the $Ar/H_2/CH_4$ system, as shown in the group's CVI work and parallel work on CVD PyC,[13,14] where lower-activity species are dominant at low residence times and the formation of higher-order reactive hydrocarbons occurs as residence time increases. Therefore, the impact of residence time on densification behavior seems most important when residence time affects the reactivity of the gas phase. In the case of H_2/MTS for CVI SiC, residence time appears to impact the stoichiometry of the growing matrix, but does not appear to affect the overall densification behavior (backfilling *vs.* skinning) or densification rate significantly.

As a result of the small change in overall V/S, no significant changes in vapor growth chemistry were observed when comparing the CVD coatings and CVI matrices examined in this study. Advantageously, this enables a more direct comparison of the two processes. It is expected that process development in (relatively rapid) CVD coatings will translate well to CVI processes using the same gas system and similar volume to surface areas, thus reducing development time and costs associated with CVI operations. This study has focused on the H_2-MTS system to produce SiC, but other material systems, such as graphite (*e.g.*, $Ar–CH_4–H_2$),[50] ZrC ($ZrCl_4–CH_4–H_2$),[21,65] or Si_3N_4 ($SiCl_4–NH_3–H_2$),[66] should also benefit from the same process development design.

5 Conclusions

The vapor processing of coatings on dense substrates and the densification of porous bodies with the H_2-MTS gas system were compared, targeting the growth of crystalline SiC. The results of experimental coating and densification processes were compared to changes predicted by calculated thermodynamic equilibrium. Overall, the predicted changes were in agreement with the experimentally observed changes. The most significant deviations observed between these methods – *e.g.*, the absence of free Si in calculations – are an inherent result of CALPHAD being a closed system compared to the dynamic conditions during vapor processing. Therefore, experimental determination of kinetics-dependent variables – such as residence time – is essential in the development of vapor processing.

Presently, research on vapor processing largely treats CVD and CVI as two separate processes. While this is true as a first approximation – coatings *vs.* densifications, and different growth temperatures and run times – for a given materials system (*e.g.*, H_2-MTS), CVD and CVI are largely just different terms for the same chemical processes. The combination of CALPHAD thermodynamics analysis and rapid experimental development in CVD can be used to identify trends in process variables, avoid pitfalls in parameters, and accelerate the development of slow and thus expensive processes like CVI. Specifically, it was confirmed that CVD and CVI processes are directly comparable. This enables the use of CVD coating process changes (hours per run) to develop CVI densification processes (days to weeks per run). This condition is expected to hold true as long as changes in total volume-to-surface-area ratio between CVD and CVI processes do not result in significant changes to the dominant reaction kinetics.

In the present study, a single parameter used for CVI SiC was adjusted based on trends observed in CALPHAD and CVD SiC experiments to successfully eliminate the formation of free Si in the CVI matrix. While additional experiments are required to further increase the amount of crystalline SiC present, the trends identified in CALPHAD/CVD provide "vectors" of investigation.

Further work to reduce the development time for vapor processes will likely focus on improving the characterization workflow. In particular, identifying ways of quantifying the amounts of both crystalline and amorphous phases would assist in refining the phase boundaries defined in experimental phase diagrams, and could be used as training material for machine learning algorithms.

Conflicts of interest

There are no conflicts to declare.

Data availability

Data used in the production of this manuscript are available at DOI https://10.13139/ORNLNCCS/3007123.

Supplementary information (SI) is available. See DOI: https://doi.org/10.1039/d5ta10109c.

Acknowledgements

The authors would like to thank Dylan Richardson (NEFC Division, ORNL) for his assistance in printing binder jet SiC test pieces. This research was sponsored by the U.S. Department of Energy, Office of Fusion Energy Sciences, through the Foundational Fusion Materials R&D program LAB 24-3295 and the Fusion Materials Program under contract DE-AC05-00OR22725 with UT-Battelle, LLC. A portion of this research was also supported by the Early Career Research Program of the Office of Fusion Energy Sciences.

References

1 B. W. Lamm, T. Koyanagi, J. J. Lee, J. R. Keiser, H. Gietl and Y. Katoh, *Corros. Sci.*, 2025, **244**, 112635.
2 J. Kaufman, C. Wyckoff, B. Lam, K. Acord, T. Craigs, C. Kassner, A. Hilmas and L. Rueschhoff, *Addit. Manuf.*, 2024, **90**, 104333.
3 K. Terrani, B. Jolly and M. Trammell, *J. Am. Ceram. Soc.*, 2020, **103**, 1575–1581.
4 V. S. Sedov, A. K. Martyanov, A. A. Khomich, S. S. Savin, V. V. Voronov, R. A. Khmelnitskiy, A. P. Bolshakov and V. G. Ralchenko, *Diamond Relat. Mater.*, 2019, **98**, 107520.
5 A. Tabata, Y. Komura, T. Narita and A. Kondo, *Thin Solid Films*, 2009, **517**, 3516–3519.
6 F. Langlais, F. Loumagne, D. Lespiaux, S. Schamm and R. Naslain, *J. Phys.*, 1995, **05**, C5–C112.
7 F. Loumagne, F. Langlais and R. Naslain, *J. Cryst. Growth*, 1995, **155**, 205–213.
8 F. Loumagne, F. Langlais and R. Naslain, *J. Cryst. Growth*, 1995, **155**, 198–204.
9 D. Lespiaux and F. Langlais, *Thin Solid Films*, 1995, **265**, 40–51.
10 J. Yeheskel and M. S. Dariel, *J. Am. Ceram. Soc.*, 1995, **78**, 229–232.
11 J. E. Spruiell, *Chemical Vapor Deposition of Silicon Carbide from Silicon Tetrachloride-Methane-Hydrogen Mixtures*, Report ORNL-4326, 1968.
12 M. L. Pearce and R. W. Marek, *J. Am. Ceram. Soc.*, 1968, **51**, 84–87.
13 W. Benzinger, A. Becker and K. J. Hüttinger, *Carbon*, 1996, **34**, 957–966.
14 A. Becker and K. J. Hüttinger, *Carbon*, 1998, **36**, 213–224.
15 Y. Ohshita, A. Ishitani and T. Takada, *J. Cryst. Growth*, 1991, **108**, 499–507.
16 F. Langlais, C. Prebende, B. Tarride and R. Naslain, *J. Phys. Colloq*, 1989, **50**, C5–103.
17 C. Amato-Wierda and D. A. Wierda, *J. Mater. Res.*, 2000, **15**, 2414–2424.
18 J. L. Lamon, in *Handbook of Ceramic Composites*, Kluwer Academic, Boston, 2005, ch. 3, pp. 55–76.
19 T. Koyanagi, X. Hu, C. M. Petrie, G. Singh, C. Ang, C. P. Deck, W.-J. Kim, D. Kim, C. Sauder, J. Braun and Y. Katoh, *J. Nucl. Mater.*, 2024, **588**, 154784.
20 V. Ramanuj, R. Sankaran, B. Jolly, A. Schumacher and D. Mitchell, *J. Am. Ceram. Soc.*, 2021, **105**, 2421–2441.
21 B. W. Lamm, J. W. McMurray, E. Cakmak, M. J. Lance and D. J. Mitchell, *Surf. Coat. Technol.*, 2022, **444**, 128672.
22 N. Kunioshi, S. Hagino, A. Fuwa and K. Yamaguchi, *Appl. Surf. Sci.*, 2018, **441**, 773–779.
23 N. Kunioshi, Y. Moriyama and A. Fuwa, *Int. J. Chem. Kinet.*, 2016, **48**, 45–57.
24 S. Ravasio, M. Masi and C. Cavallotti, *J. Phys. Chem. A*, 2013, **117**, 5221–5231.
25 H. Rauscher, *Surf. Sci. Rep.*, 2001, **42**, 207–328.
26 F. Loumagne, F. Langlais and R. Naslain, *J. Phys. IV*, 1993, **3**, C3–533.
27 C. Y. Tsai, S. B. Desu and C. C. Chiu, *J. Mater. Res.*, 1994, **9**, 104–111.
28 A. Josiek and F. Langlais, *J. Cryst. Growth*, 1996, **160**, 253–260.
29 T. Kaneko, H. Sone, N. Miyakawa and M. Naka, *Jpn. J. Appl. Phys.*, 1999, **38**, 2089–2091.
30 B. A. Weinstein and G. J. Piermarini, *Phys. Rev. B*, 1975, **12**, 1172–1186.
31 I. Iatsunskyi, G. Nowaczyk, S. Jurga, V. Fedorenko, M. Pavlenko and V. Smyntyna, *Optik*, 2015, **126**, 1650–1655.
32 S. i. Nakashima, M. Higashihira, K. Maeda and H. Tanaka, *J. Am. Ceram. Soc.*, 2002, **86**, 823–829.
33 Y. Gallou, M. Dubois, A. Potier and D. Chaussende, *Acta Mater.*, 2023, **259**, 119274.
34 S. Nakashima, K. Kisoda, H. Niizuma and H. Harima, *Phys. B*, 1996, **219–220**, 371–373.
35 S. Sorieul, J. M. Costantini, L. Gosmain, L. Thomé and J. J. Grob, *J. Phys.: Condens. Matter*, 2006, **18**, 5235–5251.

36 F. Tuinstra and J. L. Koenig, *J. Chem. Phys.*, 1970, **53**, 1126–1130.
37 D. S. Knight and W. B. White, *J. Mater. Res.*, 1989, **4**, 385–393.
38 S. Rohmfeld, M. Hundhausen and L. Ley, *Phys. Status Solidi B*, 1999, **215**, 115–119.
39 M. Zimbone, A. Sarikov, C. Bongiorno, A. Marzegalli, V. Scuderi, C. Calabretta, L. Miglio and F. La Via, *Acta Mater.*, 2021, **213**, 116915.
40 V. L. Christensen, A. R. Ericks, R. Silverstein, I. N. Duan and F. W. Zok, *J. Am. Ceram. Soc.*, 2024, **107**, 7086–7104.
41 J. Peng, N. S. H. Gunda, C. A. Bridges, S. Lee, J. A. Haynes and D. Shin, *Comput. Mater. Sci.*, 2022, **210**, 111034.
42 D. P. Stinton, A. J. Caputo and R. A. Lowden, *Am. Ceram. Soc. Bull.*, 1986, **65**, 347–350.
43 F. Loumagne, F. Langlais, R. Naslain, S. Schamm, D. Dorignac and J. Sévely, *Thin Solid Films*, 1995, **254**, 75–82.
44 J. Chin, P. K. Gantzel and R. G. Hudson, *Thin Solid Films*, 1977, **40**, 57–72.
45 J. I. Federer, *Fluidized Bed Deposition and Evaluation of Silicon Carbide Coatings on Microspheres, Report ORNL/TM-5152*, ORNL, Oak Ridge, TN, 1977.
46 K. Minato and K. Fukuda, *J. Mater. Sci.*, 1988, **23**, 699–706.
47 B. J. Choi and D. R. Kim, *J. Mater. Sci. Lett.*, 1991, **10**, 860–862.
48 S. Motojima and M. Hasegawa, *Thin Solid Films*, 1990, **186**, L39–L45.
49 G. D. Papasouliotis and S. V. Sotirchos, *MRS Proceedings*, 1993, **334**.
50 W. Benzinger and K. J. Hüttinger, *Carbon*, 1996, **34**, 1465–1471.
51 C. D. Stinespring and J. C. Wormhoudt, *J. Appl. Phys.*, 1989, **65**, 1733–1742.
52 R. N. Ghoshtagore and R. L. Coble, *Phys. Rev.*, 1966, **143**, 623–626.
53 J. D. Hong and R. F. Davis, *J. Am. Ceram. Soc.*, 1980, **63**, 546–552.
54 J. D. Hong, R. F. Davis and D. E. Newbury, *J. Mater. Sci.*, 1981, **16**, 2485–2494.
55 T. Takai, T. Halicioğlu and W. A. Tiller, *Surf. Sci.*, 1985, **164**, 327–340.
56 T. Koyanagi, M. J. Lance and Y. Katoh, *Scripta Mater.*, 2016, **125**, 58–62.
57 G. D. Papasouliotis and S. V. Sotirchos, *J. Electrochem. Soc.*, 1994, **141**, 1599–1611.
58 G. Gouadec and P. Colomban, *Prog. Cryst. Growth Charact. Mater.*, 2007, **53**, 1–56.
59 K. Stewart, B. Lamm and T. Koyanagi, *Int. J. Appl. Ceram. Technol.*, 2025, **22**, e15032.
60 A. Becker and K. J. Hüttinger, *Carbon*, 1998, **36**, 225–232.
61 W. Benzinger and K. J. Hüttinger, *Carbon*, 1998, **36**, 1033–1042.
62 G. F. Froment, K. B. Bischoff and J. de Wilde, in *Chemical Reactor Analysis and Design*, John Wiley & Sons, Inc, 3rd edn, 2011, ch. 3, pp. 152–239.
63 Z. Hu and K. J. Hüttinger, *Carbon*, 2001, **39**, 1023–1032.
64 W. Zhang and K. J. Hüttinger, *Carbon*, 2001, **39**, 1013–1022.
65 B. W. Lamm and D. J. Mitchell, *Coatings*, 2023, **13**, 266–296.
66 K. Niihara and T. Hirai, *J. Mater. Sci.*, 1976, **11**, 593–603.

